Heat transfer of a large-scale water pit heat storage under transient operations

Xiang, Yutong; Gao, Meng; Furbo, Simon; Wang, Dengjia; Tian, Zhiyong; Fan, Jianhua

Published in:
Journal of Energy Storage

Link to article, DOI:
10.1016/j.est.2022.105455

Publication date:
2022

Document Version
Publisher's PDF, also known as Version of record

Journal of Energy Storage 55 (2022) 105455

Contents lists available at ScienceDirect

Journal of Energy Storage

journal homepage: www.elsevier.com/locate/est

Research Papers

Heat transfer of a large-scale water pit heat storage under transient operations

Yutong Xiang [a], Meng Gao [a], Simon Furbo [a], Dengjia Wang [b], Zhiyong Tian [c], Jianhua Fan [a,*]

[a] Department of Civil Engineering, Technical University of Denmark, Brovej 118, Kgs. Lyngby DK 2800, Denmark
[b] State Key Laboratory of Green Building in Western China, Xi'an University of Architecture and Technology, Xi'an, Shaanxi 710055, China
[c] School of Environmental Science and Engineering, Huazhong University of Science and Technology, Wuhan 430074, China

ARTICLE INFO

Keywords:
Pit thermal energy storage
Computational fluid dynamics
Multi-node model
Grid size
Thermocline
Thermal stratification

ABSTRACT

An accurate and less time demanding model is required when integrating pit thermal energy storage (PTES) into solar heating systems. Multi-node (1D) models are commonly used, but these models face challenges when calculating PTES thermal stratification and heat loss. Therefore, a full-scale computational fluid dynamics (CFD) model of PTES inclusive water and soil regions is developed using FLUENT to improve the accuracy of heat transfer calculation of a multi-node model. The CFD model is validated against the Dronninglund PTES measurements regarding PTES thermal stratification, inlet/outlet energy flow, and soil temperature distribution. The model corresponds well to the measurements in three aspects: (i) a maximum temperature difference of 1 K in the water region; (ii) a maximum temperature difference of 2 K in the soil region; (iii) a maximum outlet temperature difference of 3 K. An indicator $R_{\Delta T/\delta}$ defined as the ratio between the thermocline temperature difference and the thermocline thickness is proposed to assess suitable grid size for PTES models, and the quantitative relationship between $R_{\Delta T/\delta}$ and grid size is recommended. Investigations with a range of grid sizes show that by using the recommended grid size, the prediction accuracy of the multi-node model TRNSYS Type 343 is significantly improved. The root mean square deviations of the predicted MIX number are decreased by 11–43 % for different years, and the relative differences of the monthly charge/discharge energy from the measurement are within 5 %. The findings of this study provide guidance for selecting appropriate grid sizes to achieve better calculation accuracy for large-scale PTES.

1. Introduction

In compliance with the Paris Agreement, rapid uptake of renewable energies is necessary [1]. Thermal energy storage technologies can be used to integrate high proportions of renewable energy in electricity generation, industry, and buildings. Therefore, thermal energy storage is a critical component of the energy transition investment package and receives increasing attention [1].

Water-based large-scale heat storage has experienced rapid development over the last decade for three reasons: 1) Large-scale thermal energy storage outperforms economically small-scale thermal energy storage, especially when the storage size exceeds 10,000 m^3 [2–5]; 2) The increase in storage volume can reduce heat losses per m^3 storage volume by lowering surface area/volume ratios [6,7]; 3) Water has a high thermal capacity and a simple thermal storage structure that can be used [8,9].

Commonly, the most used types of large-scale thermal energy storage in practical applications can be divided into the following [10]: tank thermal energy storage (TTES), borehole thermal energy storage (BTES), aquifer thermal energy storage (ATES), and pit thermal energy storage (PTES). Notably, PTES is known for enabling higher charge/discharge energy rates and lower investment costs than other types [3,8]. With the successful construction and operation of large-scale PTES in Denmark, about ten projects integrated with PTES are in operation or planned [11]. The newly built PTES are partly buried under the ground level, with a height higher than 10 m and a volume larger than 10,000 m^3. In this case, three inlet/outlet diffusers are equipped for better thermal stratification. It is challenging to set up actual experiments for such a large project to investigate the factors that affect the performance of PTES. Therefore, suitable modeling tools are preferred in the planning phase. For instance, the 1D models based on the finite difference and the finite element method are prevailing among researchers due to their less computational effort.

* Corresponding author.
E-mail address: jif@byg.dtu.dk (J. Fan).

https://doi.org/10.1016/j.est.2022.105455
Received 28 May 2022; Received in revised form 28 July 2022; Accepted 8 August 2022
Available online 14 August 2022

Nomenclature

Latin characters

C_p	specific capacity, [J/kg·K]
$C_{1\varepsilon}$, C_2	turbulence constant, [−]
E	energy, [MWh]
Fr	Froude number, [−]
g	gravitational acceleration, [m/s^2]
k	turbulence kinetic energy, [kg m^2/s^2]
L	location, [m]
M	energy momentum, [J/m]
m	mass flow rate, [kg/min]
N	number of values for the simulation period, [−]
n	node number, [−]
P	parameters, [−]
T	temperature, [°C]
t	time, [s]
$R_{\Delta T/\delta}$	ratio of thermocline temperature difference to thermocline thickness, [K/m]
Re	Reynolds number, [−]
Ri	Richardson number, [−]
RMSD	root mean square deviation, [−]
u	velocity of water, [m/s]
V	volume, [m^3]
z	height from the PTES bottom, [m]

Subscripts

bottom	bottom diffuser
c	cold water
ch	charge
calc	calculated
disch	discharge
h	hot water
i	time step
meas	measured
middle	middle diffuser
top	top diffuser
s	soil
w	water

Greek

ρ	density, [kg/m^3]
λ	thermal conductivity, [W/m·K]
μ	dynamic viscosity, [kg/m·s]
τ	stress tensor, [kg/m^2·s^2]
ε	turbulent energy dissipation rate, [m^2/s^3]
δ	thermocline thickness, [m]
σ_k	turbulence kinetic energy Prandtl number, [−]
σ_ε	turbulence energy dissipation Prandtl number, [−]
Δ	difference, [−]
ϑ	relative deviation ratio, [%]
θ	dimensionless temperature, [−]

Dahash et al. [12–16] developed a model based on the finite element method. Compared to Dronninglund PTES measurements, numerical results such as annual charge/discharge energy, internal energy, and heat loss were all within 0.5 % deviation. Moreover, the calculated temperature development inside the PTES also agreed well with the measured results. However, the model was implemented on the COMSOL platform, and linking with system simulation software was not easy. In this context, further system-level investigation using this model remains a challenge.

Published models for PTES studies based on the finite difference method include Type 342, Type 343, Type 1300, Type 1322, and Type UGSTS (Underground Seasonable Thermal Energy Storage), all developed in the TRNSYS environment. Raab et al. [17] carried out a validation study for Type 342, considering measured data from the Hannover TTES. Simulation results showed that the maximum deviation over the year between calculated and measured temperatures was 3.7 K which appeared at the height of the middle charging/discharging diffuser. Type 342 was also studied by Gauthier [18] and Pan et al. [19] using Dronninglund PTES measurements. Gauthier [18] compared Type 342, Type 1300, and Type 1322 under the same conditions. The coefficients of determination for all three types of energy flow and outlet temperature were above 95 %. However, Type 342 showed significant deviations in predicting side and bottom heat losses. Pan et al. [19] modified Type 342 to consider the actual scale PTES with more than two inlet/outlets. The results showed a marked difference between the calculated and measured MIX number value between July and October, demonstrating that Type 342 overestimated mixing in the PTES. Xie et al. [20] developed a simulation model of PTES based on Type 343. The calculated yearly energy flow showed good agreement with the measurement data of the Dronninglund PTES. In addition, the influence of parameters, such as soil properties and inlet arrangement on the performance of PTES was elucidated. Bai et al. [21,22] developed the Type UGSTS and verified it by the experimental data of the Huangdicheng PTES. Good agreement was shown between the measured and the simulated results. The difference between the calculated and measured temperatures was 1.4 K for PTES and 7 K for soil temperature. Additionally, Fan et al. [23] modified a TRNSYS model to include a 75,000 m^3 PTES for the Marstal district heating plant. Compared with the measured results, the simulation could reflect the temperature development trend of PTES but failed to reproduce the inner temperature distribution, especially from May to August.

The aforementioned literature shows that PTES simulation research is still in the model validation process. Building an experimental platform is a challenge because actual PTES is large and complex in shape, and detailed studies are time-consuming. Currently, 1D models have good accuracy in predicting annual performance, and the models developed in the TRNSYS environment are suitable for system simulation. However, due to model assumptions (such as plug flow simplification, neglect of the inlet mixing effect, and the effects of natural convection), the 1D models show large deviations for several months and could not accurately calculate the temperature distribution under transient conditions [11]. If plug flow assumption is not used, artificial mixing will spread throughout the water at different time steps, which results in significant numerical diffusion when fewer nodes are used. In this case, it has been proposed to use more nodes to reduce numerical diffusion effectively [24]. Instruction for Type 342 suggested that finer spacing must be used in storage regions with large temperature gradients [25]. The method was also tried by Cody [26] on Type 4, Type 60, and Type 534. The investigation results showed that by increasing the number of nodes, the thermal stratification could be determined in the best possible way. However, using more nodes means more computation time. Therefore, adaptive node models were further proposed. For Type 38, the size of the nodes was allowed to vary with flow inlet conditions [27]. For the new model developed by Powell and Edgar [24], a dynamic changing node was used to track the thermocline. Yet, these approaches were investigated based on a small-scale water storage tank with two inlet/outlets. In such systems, the thermal stratification might differ from that observed in the large-scale PTES. Moreover, the adaptive grid model does have disadvantages since it cannot accurately represent the second thermocline caused by inner natural convection during the standby.

Thus for simulation and optimization of integrated thermal energy

systems, accurate and simplified models are required to improve computational efficiency while accurately representing the thermal behavior of PTES under transient conditions. To the authors' knowledge, no literature addresses the improvement of the 1D model for large-scale PTES in terms of the grid size. Additionally, no criteria are provided for selecting the proper grid size for large-scale PTES 1D models.

The current study developed a full-scale 3D model, including water and soil regions, to fully understand the thermal behaviors of PTES under different conditions. Since it is computationally intensive, the water and soil regions of the model were validated separately using measured data from the Dronninglund PTES. In this context, a four-year calculation was performed for the soil region, while four representative cases from 2017 were selected for the water region. Then, the focus was on the grid sizes in terms of calculation accuracy for PTES temperature distribution. The ratio of thermocline temperature difference to thermocline thickness was proposed as an indicator for selecting the appropriate grid size. Based on this finding, the year-round variation of the thermocline characteristic was analyzed to determine the grid size distribution for 1D models. Lastly, a three-year calculation was carried out using TRNSYS Type 343 to demonstrate the reliability of the recommended grid size distribution. The improvement was addressed by comparing the model accuracy in terms of MIX number and charge/discharge energy under different grid size distributions.

2. Numerical and experimental methodology

2.1. Pit thermal energy storage description

The 60,000 m^3 PTES of the Dronninglund plant was selected as the experimental case for validating the numerical model. Fig. 1 shows a schematic of Dronninglund PTES, which is partly constructed as a truncated pyramid stump above the ground level. The depth of the PTES is 16 m, and the sidewalls have a slope of 26.6°. The outer dimensions of the top and the bottom surface are 90 m × 90 m and 26 m × 26 m, respectively [28,29]. On the top of the PTES, there is a floating lid consisting of five layers: (from top to bottom) 1.5 mm HDPE Geomembrane, 3 mm Hypernet CN-E, 240 mm Nomalén insulation, 3 mm Hypernet HF-E, and 2 mm HDPE Geomembrane. For the side and the bottom wall, a 2.5 mm HDPE Geomembrane layer, as well as a fabric layer, are used to enclose the water [30].

Fig. 2 shows the details of the arrangements of the inlet/outlet pipes. Three 273 mm diameter inlet/outlet pipes connect the PTES through the bottom and are arranged at different height levels. In order to maintain thermal stratification inside the PTES, the inlet/outlet diffusers consist of two horizontal discs with a diameter of 2500 mm.

Accordingly, the full-scale 3D model (shown in Fig. 3), including the water and soil region, was created based on Dronninglund PTES dimensions. Two simplifications were made to simplify the mathematical models: 1) The water flow inside the leading pipe (connected to the diffusers) was neglected; 2) The supporting structure of the diffusers was ignored. Notably, the soil region was built large enough to reduce the effect of the model's adiabatic boundaries on the soil temperature distribution around the water region. In addition, the geological investigation of the Dronninglund project indicates that the groundwater level is approximately 17 m under the ground level [28,33]. Thus, the soil region was divided into two parts at the height of 17 m, each of which can be assigned different soil properties.

2.2. Mathematical model

The water region was considered an incompressible fluid with temperature-dependent thermophysical properties. In this case, the governing equations of the water region are based on the laws of conservation of mass, momentum, and energy. The upper and lower soil region had constant thermal properties, while groundwater flow was not considered to reduce the computational effort. Therefore, the governing equation of the soil region is based on the law of energy conservation.

2.2.1. Governing equations

The 3D conservations of the flow and heat transfer in the water and soil region can be defined as follows [34]:

$$\nabla \bullet (\rho_w \vec{u}) = 0 \tag{1}$$

$$\frac{\partial(\rho_w \vec{u})}{\partial t} + \nabla \bullet (\rho_w \vec{u}\vec{u}) = -\nabla p + \nabla \bullet \tau_w - \rho_w g \tag{2}$$

The enthalpy equation of the water region is shown in Eq. 3.

$$\frac{\partial(\rho_w C_{p.w} T)}{\partial t} + \nabla \cdot (\rho_w C_{p.w} \vec{u} T) = \nabla \bullet (\lambda_w \bullet \nabla T) \tag{3}$$

The enthalpy equation of the soil region is shown in Eq. 4.

$$\rho_s C_{p.s} \frac{\partial T}{\partial t} = \lambda_s \nabla^2 T \tag{4}$$

where ρ_w and ρ_s indicate the density of water and soil; u is the velocity of water; $C_{p.w}$ and $C_{p.s}$ represent the specific capacities of water and soil; λ_w and λ_s are the thermal conductivity of water and soil; τ_w presents the stress tensor of water.

2.2.2. Turbulence modeling

The flow pattern depends strongly on the configuration of the PTES (including the inlet/outlet design, the aspect ratio of the inlet/out to the storage) [35], as well as the operating conditions (such as inlet velocity, inlet temperature, the temperature difference between the incoming and internal water, and the internal stratification). Therefore, the fluid dynamic model should be selected carefully to better deal with the fluid mixing inside PTES.

The inlet *Re* number, *Fr* number, and *Ri* number (i.e., $Ri = Fr^{-2}$) have been used in previous studies as indicators by which flow state can be evaluated for different radial diffuser designs. A *Re* number criterion given by Blevins [36] predicted that for almost all full-scale tanks operating at a design flow rate, the flow entering the tank would be fully turbulent when an isothermal radial wall jet issued from a slot of finite height. Deng et al. [37] selected k-ε to study the performance of a

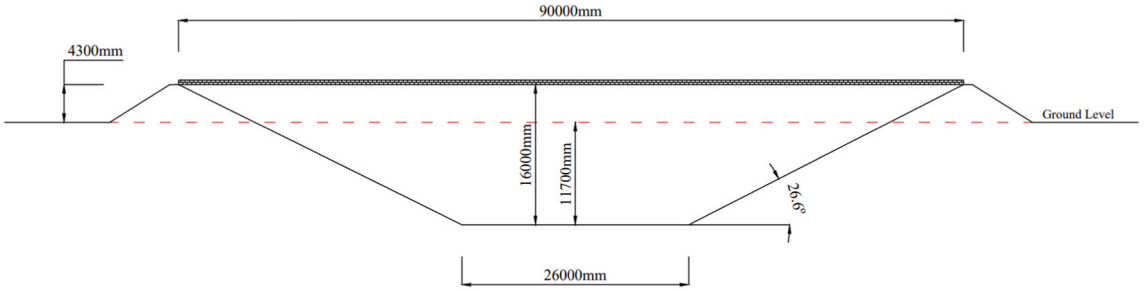

Fig. 1. Schematic of Dronninglund PTES.

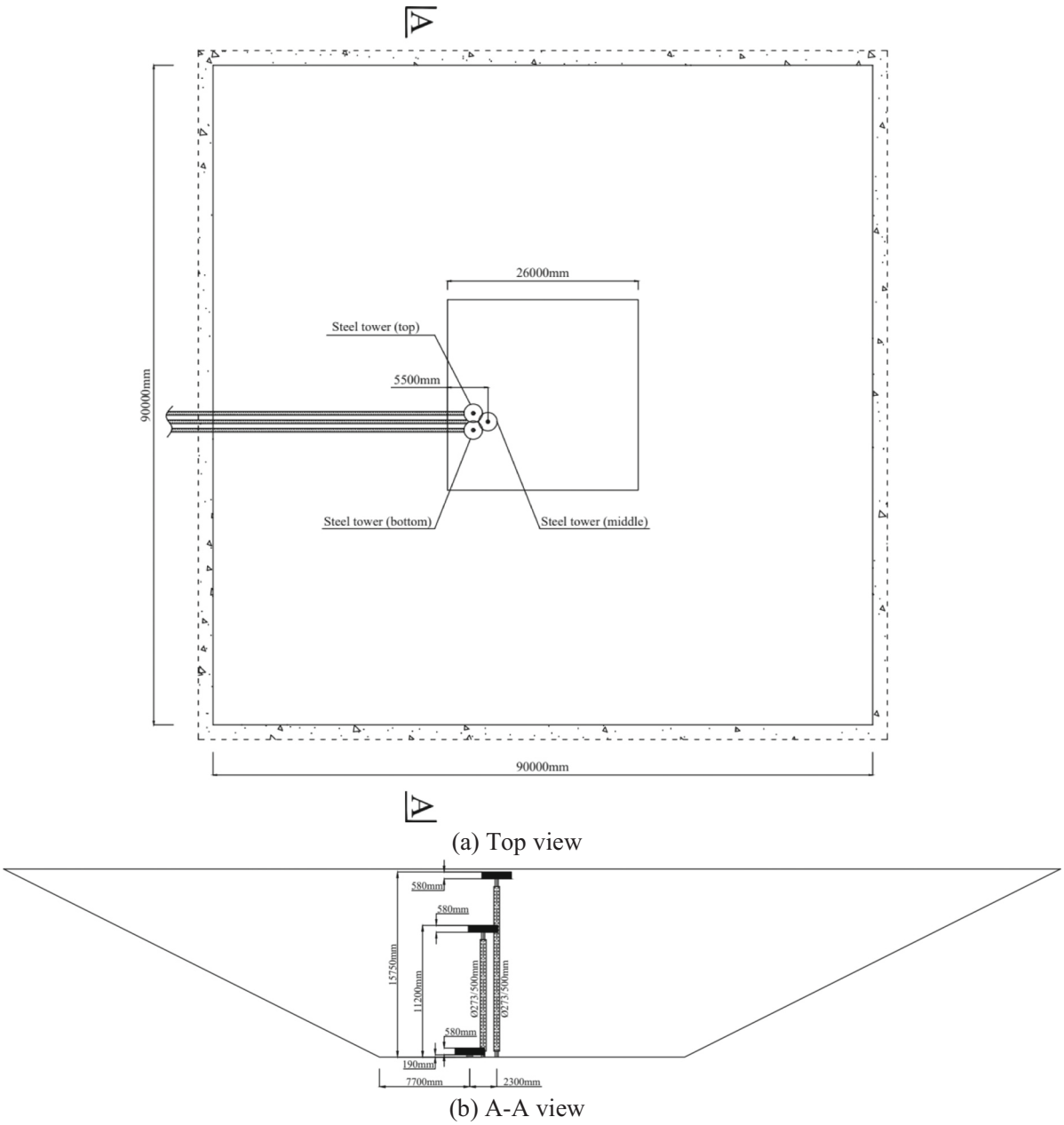

Fig. 2. Illustration of the inlet/outlet pipes arrangement inside the PTES [31,32].

thermal storage tank with radial diffusers since the *Re* number was much larger than 2300 in their study. Moreover, in the case of stratified flow, both the inlet *Re* and *Fr* number influence the turbulent transition. Keulegan [38] believed that the transition started when the ratio of *Re* number and *Ri* number exceeded 500. Investigations conducted by Cai et al. [39] also confirmed that it was essential to consider both the inlet *Fr* and *Re* number. Therefore, when the inlet *Re* number exceeds 2300, and the *Ri* number is greater than 500, it should be considered turbulent flow.

In this study, the turbulence model was used to simulate water flow inside PTES because the dynamic inlet *Re* number is more significant than 5000, and the *Ri* number is beyond 500 during most operating periods. Moreover, the realizable k-ε model was selected due to its ability to more accurately predict the spreading rate of round jets [34,40]. The transport equations in this model for the kinetic energy k and the dissipation rate ε are given as Eq. (5) and Eq. (6).

$$\frac{\partial(\rho_w k)}{\partial t}+\nabla\bullet(\rho_w kU)=\nabla\bullet\left[\left(\mu_w+\frac{\mu_t}{\sigma_k}\right)\bullet\nabla(\mathrm{k})\right]+G_k+G_b-\rho\varepsilon \tag{5}$$

$$\frac{\partial(\rho_w \varepsilon)}{\partial t}+\nabla\bullet(\rho_w \varepsilon U)=\nabla\bullet\left[\left(\mu_w+\frac{\mu_t}{\sigma_\varepsilon}\right)\bullet\nabla(\varepsilon)\right]+C_{1\varepsilon}\frac{\varepsilon}{k}C_{3\varepsilon}G_b-C_2\rho_w\frac{\varepsilon^2}{k+\sqrt{\frac{\mu_w}{\rho_w}\varepsilon}} \tag{6}$$

The turbulence constants $C_{1\varepsilon}=1.44$ $C_2=1.9$ $\sigma_k=1.0$ and $\sigma_\varepsilon=1.2$ are established according to Ref. [34].

2.3. Model details

2.3.1. Meshing

The mesh scheme plays an essential role in the rationality of the simulation results. In this study, the soil and water regions were

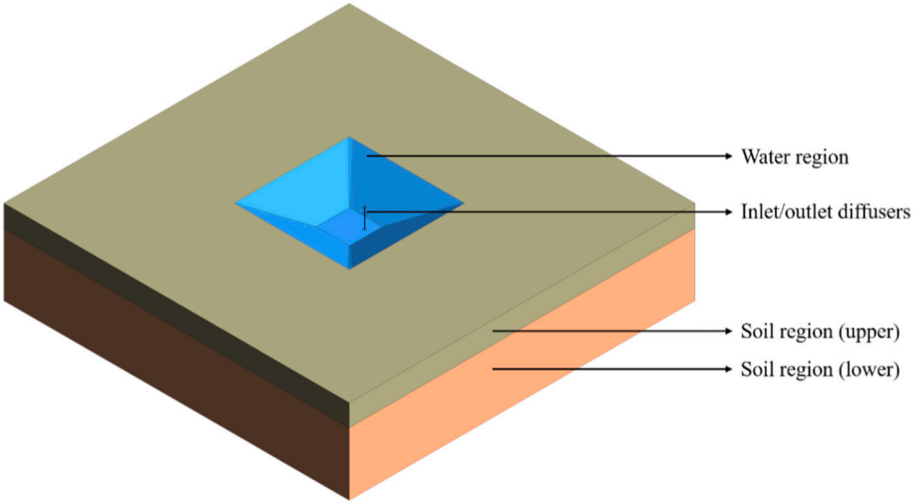

Fig. 3. 3D model of the water pit heat storage.

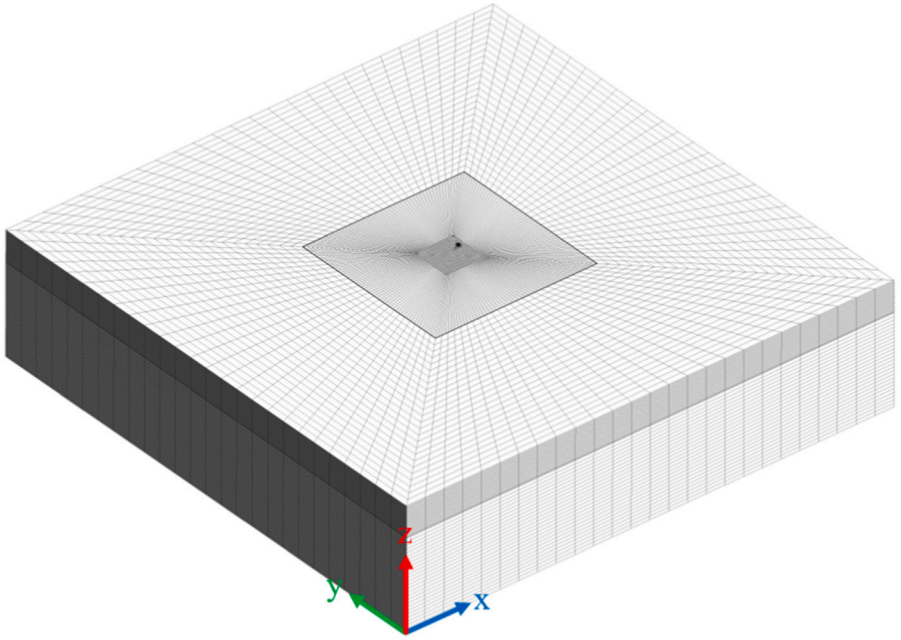

(a) Axonometric view

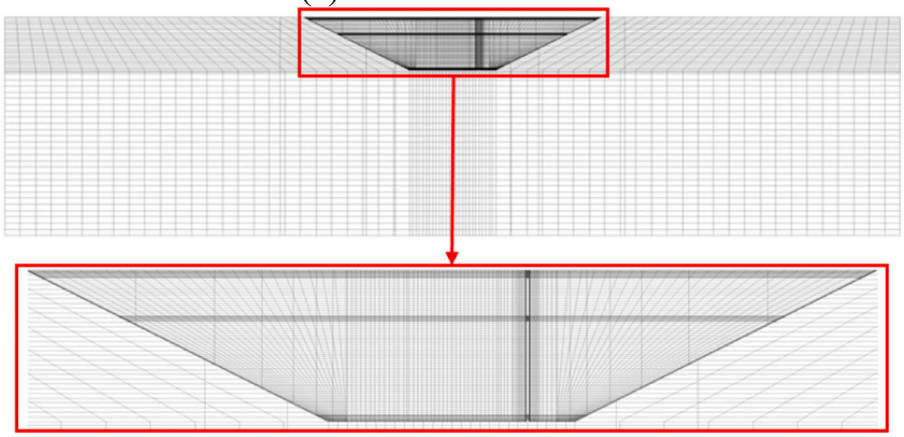

(b) Vertical cut plane

Fig. 4. Grid scheme of the model.

separated by interfaces so that the two regions could be calculated separately with different mesh densities (see Fig. 4 (a)) to reduce the calculation effort. The structure grids were used for both the water and the soil regions. It is evident in Fig. 4 (b) that mesh in the region near the inlet/outlet diffuser was refined in order to capture its relatively high temperature and velocity gradients. Additionally, a boundary layer mesh was applied close to the adjacent walls to address heat transfer between the soil and water region. With appropriate grid size, truncation and discretization errors can be minimized, facilitating faster convergence [41]. Section 3 analyzes the calculation accuracy with different grid sizes.

2.3.2. Numerical procedure

The governing equations were solved in each cell. A SIMPLE pressure-velocity coupling scheme was employed. The spatial discretization settings for pressure, momentum, and energy were PRESTO, second-order upwind, and second-order upwind, respectively. The pressure, density, momentum, and energy under relaxation value factors were 0.3, 0.8, 0.7, and 0.95, respectively. For energy, the convergence criteria were kept at 10^{-6}, while for velocity, continuity, and other variables, it was kept at 10^{-3}.

2.3.3. Thermal properties

Water was used as the heat storage media inside PTES. The following correlations provide the temperature dependence of the density, dynamic viscosity, thermal conductivity, thermal expansion coefficient, and specific heat capacity of water, respectively [42,43], where T is temperature in Kelvin.

Density, $[kg/m^3]$

$$\rho = 863 + 1.21*T - 2.57*10^{-3}*T^2 \quad (7)$$

Dynamic viscosity, [kg/m·s]

$$\mu = 9.67*10^{-2} - 8.207*10^{-4}*T + 2.344*10^{-6}*T^2 - 2.244*10^{-9}*T^3 \quad (8)$$

Thermal conductivity, [W/m·K]

$$\lambda = 3.75*10^{-1} + 8.84*10^{-4}*T \quad (9)$$

Specific heat, [J/kg·K]

$$C_p = 4432.6 - 1.819*T + 3.3*10^{-3}*T^2 \quad (10)$$

According to the geological survey and reported soil properties [44–46], the soil properties for different parts are shown in Table 1, together with the physical properties of other solid materials used in this study [13,47–50]. The thermal conductivity of Nomalén 28 N was assumed to be 0.02 higher than the standard value of 0.04 W/(m·K) [20,51], considering the 30 % to 50 % increase in thermal conductivity due to degradation of the insulation material caused by a long time exposure to high temperature and humidity.

2.4. Monitoring parameters

The distribution of the temperature measuring points in the Dronninglund PTES and the soil region can be seen in Fig. 5 [18,52]. Notably, all dimensions are in millimeters in the schematic diagram. In addition to the top sensor located 0.1 m under the bottom of the cover, 32 temperature sensors are installed with an interval of 0.5 m from the bottom to the top of the PTES. On the north side of the PTES, four temperature sensors are placed in the soil at a depth of 10 m, 15 m, 20 m, and 25 m with the aim of monitoring soil temperature changes. Further, three inlet/outlet pipes are equipped with sensors that measure the water's temperature and volume flow rate. The measured temperatures are used to validate the developed CFD model.

Table 1
Physical properties of solid materials used in the numerical model.

Material	ρ [kg/m^3]	λ [W/m·K]	C_p [J/kg·K]
Soil (upper part)	1840	1.8	900
Soil (lower part)	2200	2.3	1800
Nomalén 28 N	28	0.06	2857
HDPE	940	0.4	1900
HF-E	940	0.4	1900
Stainless Steel	7600	15	490

3. Results and discussion

3.1. Uncertainty and calibration indicators

Before the validation process, it is essential to outline all uncertainties that arise from the measurements and the modeling approach.

The measurement uncertainties are owed to measurement equipment's accuracy and measurement method. In the Dronninglund project, the temperature sensors are Class A PT100, with an accuracy of ±0.15 K [53]. The volume flow rate is measured using electromagnetic flowmeters, with an accuracy of 0.4 %. It is worth noting that the position of temperature sensors inside the PTES may change as the water level fluctuates. In addition, the inlet/outlet temperatures and volume flow rate are measured in the technical room a distance away from the PTES. Therefore, it takes time for the fluid in the leading pipes to flow between the PTES and the technical room, resulting in delay and inaccurate temperature measurements in case of frequent operation mode shifts [20].

The modeling uncertainties are related to the model assumptions. In this study, the water level is assumed constant, and the water enters the PTES directly from the diffusers without considering the flow process in the leading pipe. Additionally, the thermal properties of insulation and soil are constant regardless of changes in moisture content.

By comparing the calculated and the measured parameters, root mean square deviation (RMSD) is used. RMSD is defined as Eq. (11).

$$\mathrm{RMSD} = \sqrt{\frac{1}{N}\sum_{i=1}^{N}\left(P_{calc,i} - P_{meas,i}\right)^2} \quad (11)$$

where $P_{calc,\,i}$ and $P_{meas,\,i}$ are respectively the calculated and the measured parameters logged every 10 min. N presents the number of obtained values for the simulation period.

3.2. Soil region

The calculation of the 3D model combining the soil and water region is very time-consuming due to the large volume and the calculation principle of the water region. Therefore, the 3D model of the soil region was tested separately under long-term simulations to find a suitable grid. Seven grid densities were formed by refining the mesh in different directions. The calculated soil temperatures were compared with the measured temperatures from 05/2014 to 12/2017.

Fig. 6 illustrates the soil temperature variations at different locations. The discontinuity in the measurement results is due to a hardware failure of the SCADA system [52]. Overall, the model can reflect the development of measured soil temperatures. Even though the calculated soil temperatures at 15 m and 20 m are slightly different from the measured temperature, this can be explained by the change of soil thermal properties over time due to changes in soil moisture. The maximum differences between the measured and calculated soil temperatures at 10 m, 15 m, 20 m, and 25 m are 2 K, 1.8 K, 1.6 K, and 0.8 K, respectively. Moreover, the soil temperature calculation with different grid densities is basically unbiased, which means that increasing node numbers does not affect the calculated temperatures in the soil region.

Therefore, the heat transfer prediction accuracy of the surrounding soil model is considered acceptable. To reduce the computational

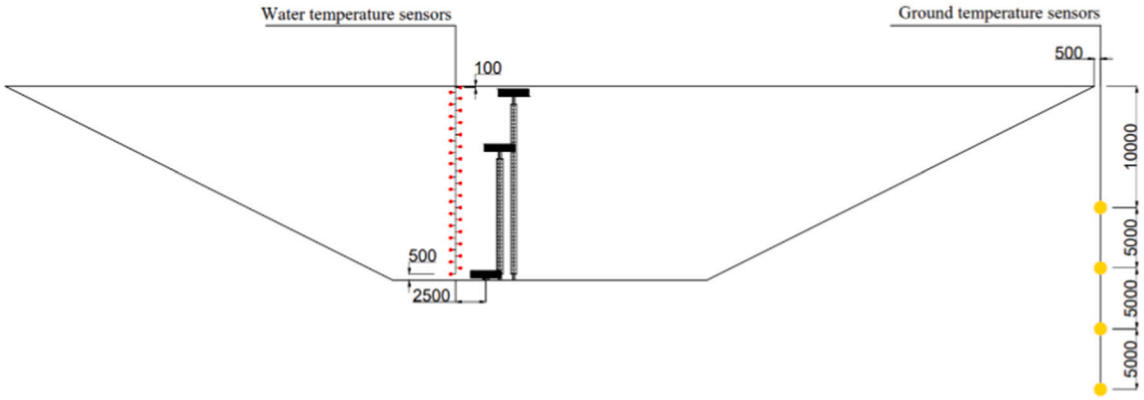

Fig. 5. Scheme diagram of monitoring sensor position.

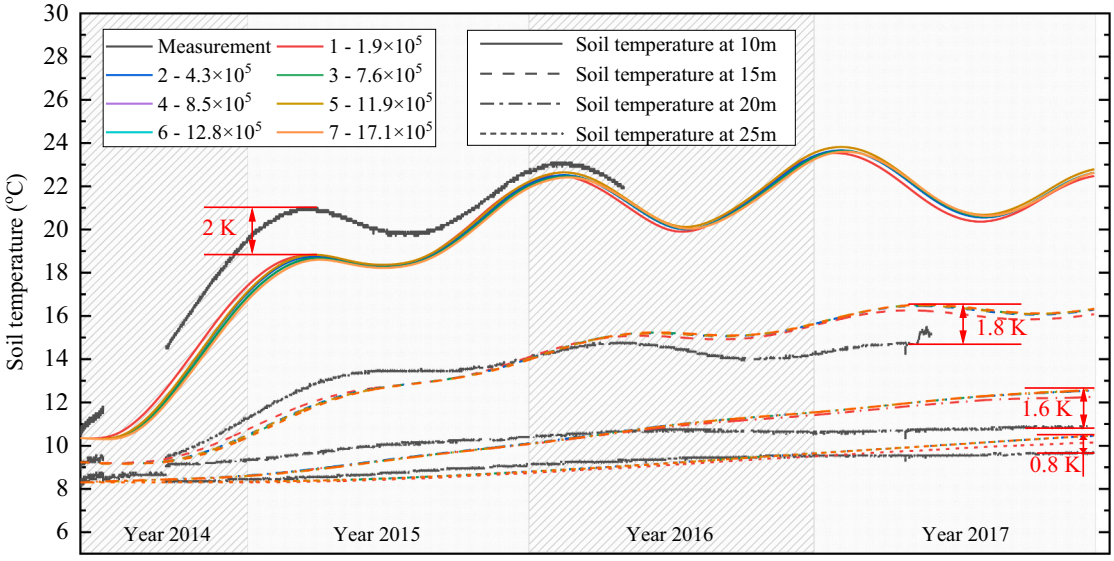

Fig. 6. Soil temperature calculation for 7 mesh densities.

requirements, a grid with 1.9×10^5 nodes was used for the soil-water combination model simulation.

3.3. Water region

3.3.1. Representative period selection

The charging/discharging conditions and the thermal stratification inside the PTES constantly change over the year. However, it is difficult to perform long-term simulations for such a large 3D soil-water combination model due to the limitation of computing resources. Therefore, four representative cases in the year 2017 were selected to assess the accuracy of the 3D model, considering thermal stratification, charging/discharging characteristics, and the heat transfer between the water and soil region. Fig. 7 shows the changes in PTES temperature distribution and operating conditions over 24 h for the four cases. For Case 1, PTES temperature distribution barely changed over 24 h, as is the PTES discharged at a mass flow rate below 15 kg/m^3 for most of the day. For Case 2, the temperature distribution at heights above 13 m varies greatly between 10:00 and 16:00 due to charge with a mass flow rate greater than 90 kg/m^3. For Case 3, the PTES temperature distribution does not change much either, but a significant temperature gradient is clearly seen between the heights of 14 m and 15 m. All heights of Case 4 have a slight temperature increase due to the inflow of hot water from the middle and top diffusers during the daytime.

Table 2 summarizes the operating conditions and thermocline characteristics. It is worth noting that, for Case 2, the thermocline thickness is decreasing, and the thermocline temperature difference is increasing from 16:00. The dimensionless temperature, defined by Eq. (12), is used to assess the thermocline thickness [26].

$$\theta(z) = \frac{T(z) - T_c}{T_h - T_c} \tag{12}$$

In Eq. (12) $\theta(z)$ is the dimensionless temperature, $T(z)$ is the average warm/cold water temperature at a certain height inside PTES, T_h is the PTES hottest temperature and T_c is the PTES coldest temperature.

The thermocline is defined where the dimensionless temperature is in the range 0.15–0.85 [54]. In this context, the thermocline thickness is calculated using Eq. (13). In the equation, z_h is the height where $\theta = 0.85$ and z_c is the height where $\theta = 0.15$.

$$\Delta z = z_h - z_c \tag{13}$$

3.3.2. Effect of simulation time step and grid size

Firstly, all cases were investigated to determine the optimal time step and grid density. Fixed time steps of 0.5 s, 1 s, 1.5 s, and 2 s were tried, and the difference between calculated and measured results was less than 1 % as the time step was decreased. Subsequently, the 2 s time step was used to save computing time. Then, seven grid densities were formed by refining the grid from the z-direction and x/y direction. With

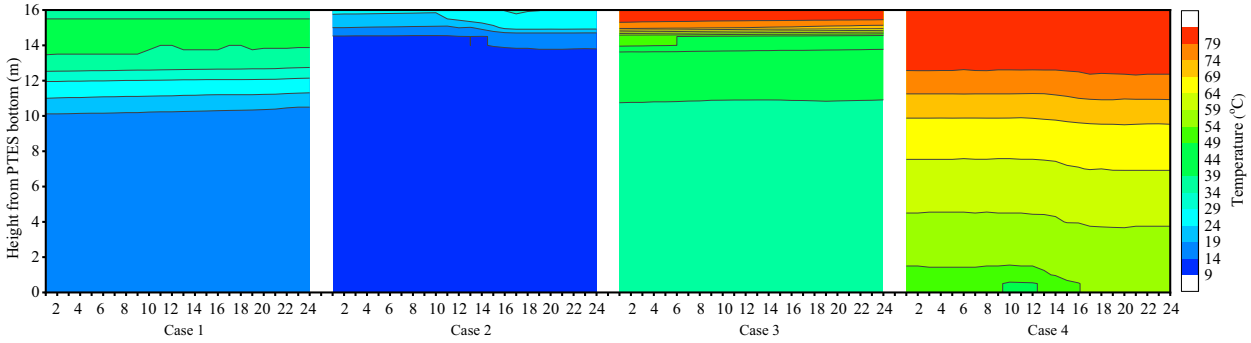

(a) Measured PTES temperature distribution

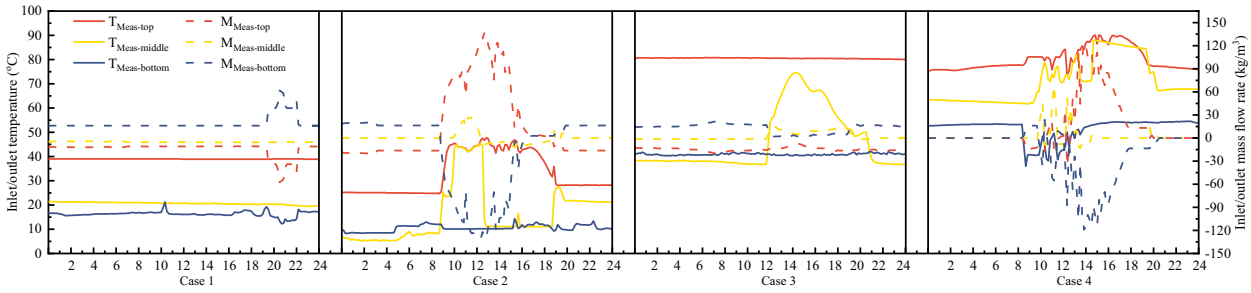

(b) Mass flow rates and temperatures of the three diffusers during the day

Fig. 7. Cases description.

Table 2
Characterization of different cases.

Case	Date	Mode	Operation condition	Thermocline description
Case 1	January 5	Discharge	Flow out from top and bottom diffusers; Flow into middle diffuser;	Thermocline thickness: 3.5 m (basically unchanged the whole day); Thermocline temperature difference: 18.8 K (basically unchanged the whole day);
Case 2	March 15	Charge (daytime)	Flow out from bottom diffuser; Flow into top and middle diffusers;	Thermocline thickness: (2.5 m from 0:00, 1.8 m start 16:00); Thermocline temperature difference: (10.5 K from 0:00, 13.8 K start 16:00);
		Discharge (nighttime)	Flow out from top diffuser; Flow into bottom diffuser;	
Case 3	June 2	Discharge (daytime)	Flow out from top diffuser; Flow into middle diffuser;	Thermocline thickness: 2 m (basically unchanged the whole day); Thermocline temperature difference: 31.4 K (basically unchanged the whole day);
		Discharge (nighttime)	Flow out from top diffuser; Flow into bottom diffuser;	
Case 4	September 1	Charge (daytime)	Flow out from bottom diffuser; Flow into the top and middle diffusers;	Thermocline thickness: 9.5 m (basically unchanged the whole day); Thermocline temperature difference: 21 K (basically unchanged the whole day);
		Standby (nighttime)	–	

the increase of the grid density in the x/y direction, the change in the calculation results is negligible. However, the grid size in the z-direction (vertical direction) significantly influences the accuracy of PTES temperature prediction. Fig. 8 presents PTES temperature distribution calculation accuracy under different grid sizes using RMSD. Notably, the thermocline region is marked between the solid black lines, as previous investigations have shown that assigning a large number of grids to the thermocline region can effectively achieve higher accuracy [24,26].

From Fig. 8, it is apparent that the grid size is negligible for temperature calculation accuracy in non-thermocline regions. Also, for non-thermocline heights, the RMSD over 24 h of simulation is within 1 K. However, for these cases, the grid size influences the accuracy of temperature calculation within the thermocline region differently. For Case 1, the temperature calculation accuracy in the thermocline region improves slightly within 0.4 K as the grid size decreases. For Case 2 and Case 3, the PTES temperature in the thermocline region is significantly overestimated at large grid sizes, with the RMSD of approximately 1.9 K and 6.8 K for the 24-h simulation, respectively. When the grid size is reduced to 0.04 m, the temperature calculation accuracy is improved by 1 K for Case2 and 3.2 K for Case 3. While the calculation results of Case 4 are independent of the grid size. In other words, for Case 4, grid size has little impact on temperature calculation accuracy.

To balance calculation accuracy and computational cost, a grid size of 0.06 m in the z-direction is used for all cases in the following study to demonstrate the model's reliability.

3.3.3. *Water temperature*

To further demonstrate the model's accuracy in calculating the PTES temperature development trend, Fig. 9 visually shows the calculated and measured temperature development inside PTES with hourly resolution. The labels marked with 'Calc' and 'Meas' represent the calculated and the measured temperature at the corresponding heights. Only the heights mentioned above have greater fluctuation over a 24-h period are plotted.

Fig. 9 shows a remarkable matching between calculated and measured PTES temperature for Case 1 and Case 4, with maximum

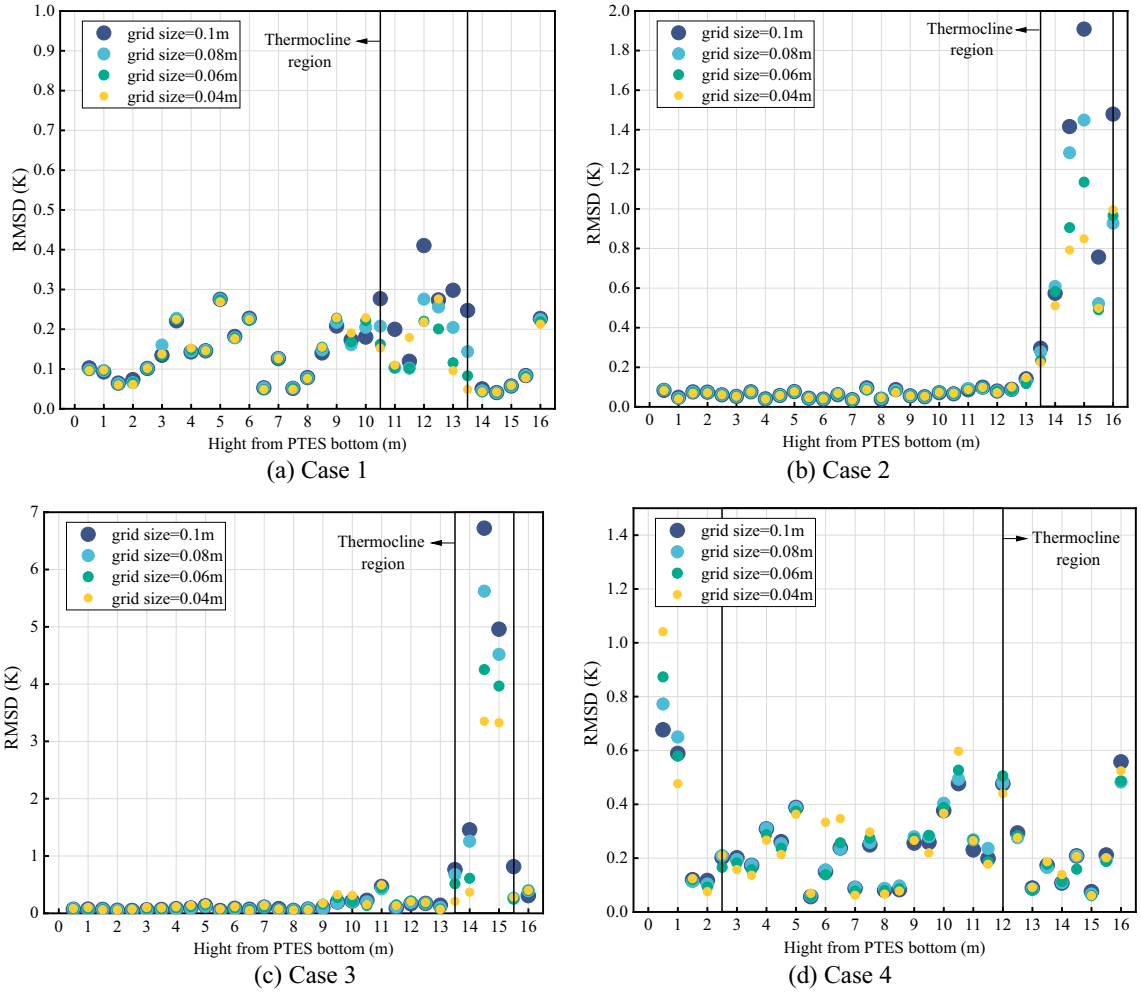

Fig. 8. Effect of grid size on the calculation accuracy.

temperature difference within 0.5 K and 1 K, respectively. However, for Case 2 and Case 3, a temperature difference larger than 2 K appeared at 14.5 m and 15 m. Two reasons can explain this:

1) The monitored temperature points inside PTES are assumed to be fixed in the CFD calculation. In contrast, the uncertainty of the actual temperature sensor position varies within ±0.3 m due to the water contraction and expansion. In this case, calculated temperatures at 14.4 m and 15.05 m are added, revealing that the calculated accuracy can be improved by considering the uncertainty of temperature measurement.
2) There is a considerable temperature difference within a smaller thickness. Together with Table 2, the temperature difference to thickness ratio (temperature gradient) for Case 2 changed from 4.2 at 14:00 to 7.7, while it reached 15.7 for Case 3 at the start of the day. In this context, two measurement points are not enough to reflect the actual temperature gradient within such a large ratio because the temperature of the adjacent heights has a significant impact on its temperature prediction.

3.3.4. Charging/discharging conditions

In addition to the PTES temperature distribution, the charge/discharge energy under transient calculation can also be used to examine the model accuracy. In view of the fact that the charge/discharge energy is calculated using the inlet/outlet mass flow rate and temperature, Fig. 10 presents the hourly inlet/outlet temperature and mass flow rate variation under different cases.

Slight deviations can be observed in the calculation results compared to the measurements. The maximum difference between the calculation and measurement is within 3 K for temperature and 10 kg/m^3 for mass flow rate. The calculation accuracy is acceptable considering the differences between the actual measured and calculated positions of the inlet/outlet sensors and uncertainties of the measurement in case of frequent shifts of operation mode [20].

Moreover, it is found that the outlet temperature is influenced by the temperature distribution near the outlet diffusers. In other words, the accuracy of the outlet temperature calculation will depend on the prediction of PTES temperature distribution since the calculated outlet temperature is a mixture of the temperatures near the diffusers. Therefore, it is recommended to set more measuring sensors along the PTES height to precisely capture the temperatures near the diffusers.

3.4. Discussion

Overall, it can be concluded that the developed 3D model is adequate to predict the thermal performance of a large-scale PTES.

Furthermore, it is important to note that the main factor affecting the accuracy of PTES temperature calculation is the thermocline's temperature rather than the thermocline's position. The results show that Case 2 and Case 3 have almost the same thermocline position between 13.5 m and 16 m, but the RMSD of Case 3 is roughly three times that of Case 2 due to more significant temperature differences.

Therefore the temperature gradient, $R_{\Delta T/\delta}$, defined as the ratio of thermocline temperature difference to thermocline thickness, is

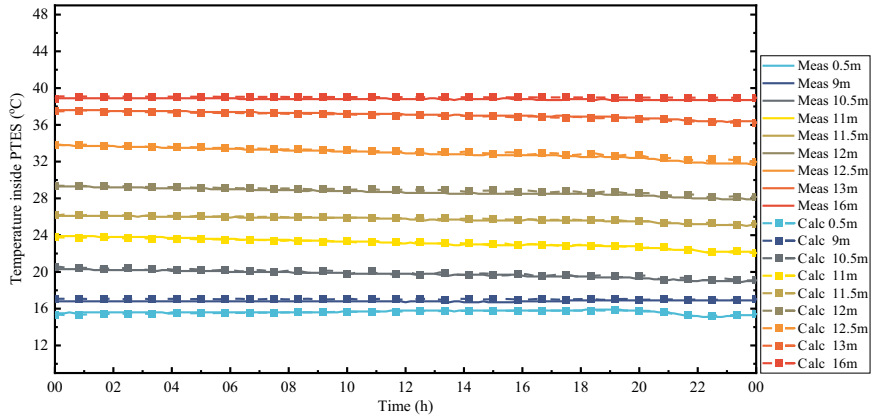

(a) Case 1

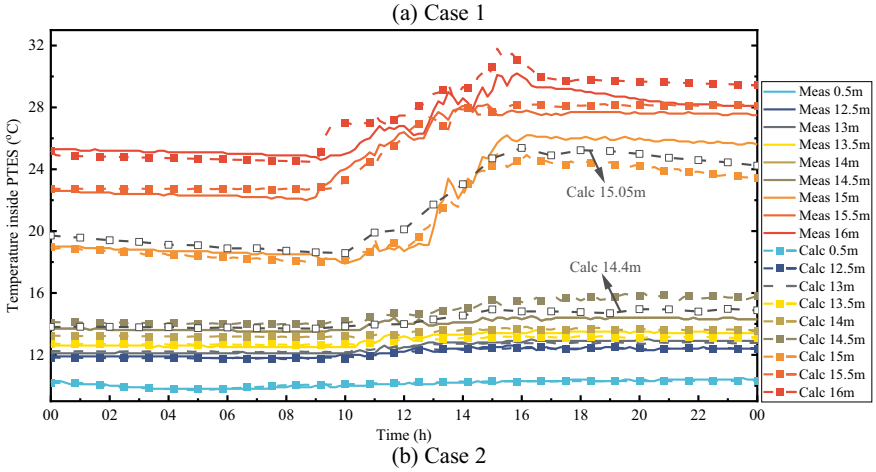

(b) Case 2

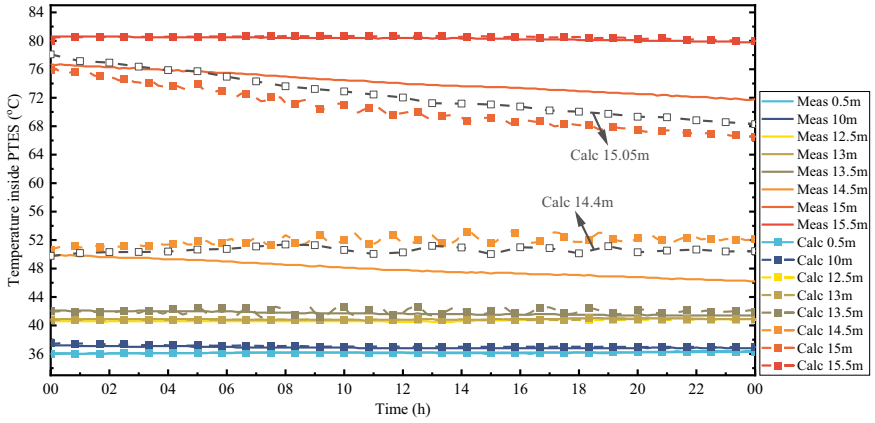

(c) Case 3

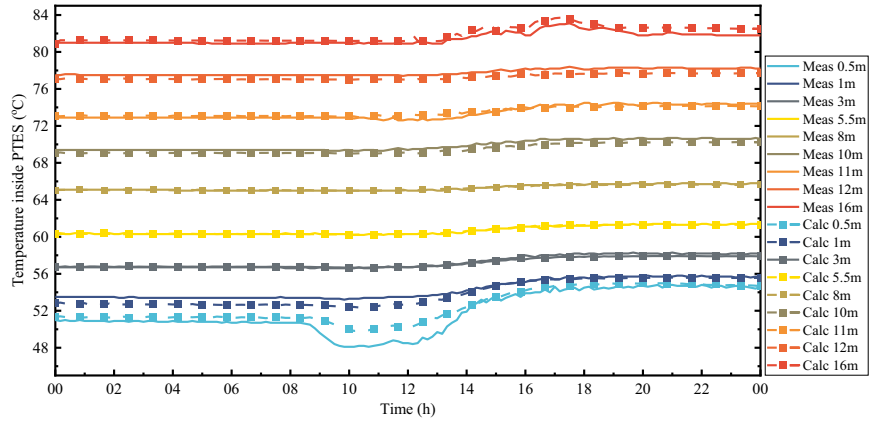

(d) Case 4

Fig. 9. Comparison of PTES calculated and measured temperatures with hourly resolution.

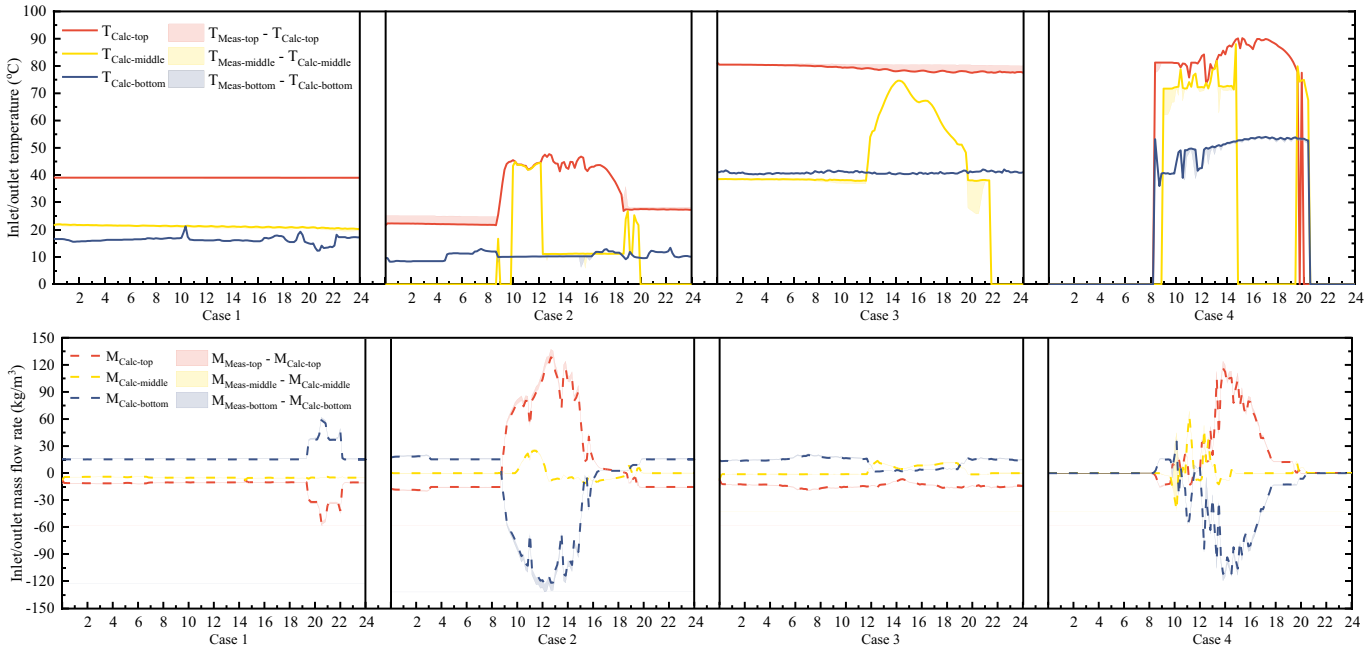

Fig. 10. Comparison of charging/discharging conditions with hourly resolution.

proposed in this study. $R_{\Delta T/\delta}$ can be used to guide the selection of suitable grid sizes for 1D models. For a higher calculation accuracy, the recommended grid sizes are summarized as follows, depending on $R_{\Delta T/\delta}$:

1) A grid size of 0.1 m is recommended when $R_{\Delta T/\delta}$ is lower than 5 K/m.
2) A grid size of 0.06 m is recommended when $R_{\Delta T/\delta}$ is between 5 and 7 K/m.
3) A grid size of 0.04 m is recommended when $R_{\Delta T/\delta}$ is larger than 7 K/m.

It is shown that a higher temperature gradient of the thermocline requires a smaller grid size, in other words, a higher number of grid points in the 1D models. The explanation is that a higher temperature gradient means larger temperature difference and/or a smaller thickness of the thermocline. In order to capture the temperature change in a small distance, a smaller grid size is needed. However, the grid shall not be too coarse or too fine, because a coarser grid will sacrifice the calculation accuracy, while an unnecessarily finer grid will significantly increase the computational cost. The recommended grid sizes aim to keep a balance between these factors.

4. Application

The appropriate grid size for different heights is chosen by analyzing yearly thermocline conditions to thoroughly verify the conclusions based on the grid size estimation obtained from the 3D model calculation. Then the improvement of model accuracy under the grid size correction is demonstrated using TRNSYS Type 343.

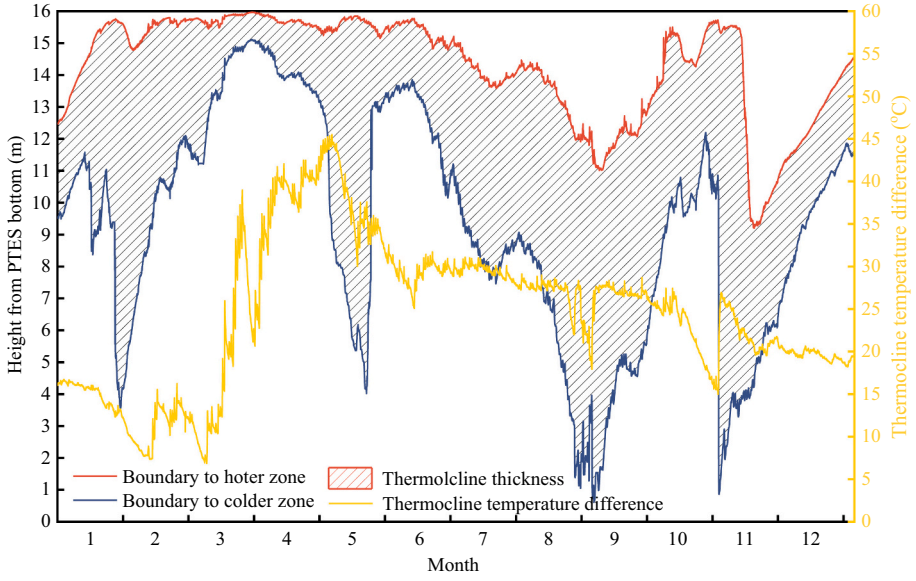

Fig. 11. Annual variation of thermocline temperature difference and thermocline thickness.

4.1. Grid size determination based on yearly thermocline characteristics

Fig. 11 shows the development of thermocline temperature difference and thermocline positions of the Dronnonglund PTES in 2017, where the thermocline thickness is highlighted with slashes. It reveals that the temperature difference increases sharply from March to May and decreases slowly from May to June since hot water is charged from the top diffuser. During this period, the thermocline is located above 13 m. From July to August, with the continuous charging, the temperature difference inside the PTES gradually decreases, resulting in a downward movement of the thermocline. Beginning in September, the dominant process turns to the discharge process, with low-temperature water entering from the bottom diffuser. In this case, the thermocline position moves upward, and the thermocline thickness gets smaller. Moreover, during the period end of October through early November, cold water of about 20 °C enters from the bottom diffuser at night, resulting in a rapid drop in the bottom water temperature.

Furthermore, the annual variation of $R_{\Delta T/\delta}$ (shown in Fig. 12) is calculated based on the annual thermocline temperature difference and thermocline thickness. Fig. 12 demonstrated that $R_{\Delta T/\delta}$ is greater than 7 in zone 1 and 2. Meanwhile, the thermocline is located above 13 m, according to Fig. 11. In addition, $R_{\Delta T/\delta}$ is between 5 and 7 for zone 3 and 4, with the thermocline located between 9 m and 15 m. Except for these zones, the $R_{\Delta T/\delta}$ is less than 5. Therefore, the grid size required for different heights for the 1D model can be summarized in Table 3 according to the recommended grid size for $R_{\Delta T/\delta}$ proposed in section 3.2.5. In this context, PTES temperature distribution and charged/discharged energy quantities are expected to be more accurate.

4.2. Improvement of TRNSYS type 343

A TRNSYS model Type 343 was developed for PTES and verified with the measurement of the Dronninglund PTES [20]. The grid size of the model is further improved by implementing the aforementioned recommendations. Calculations for different grid size distributions (listed in Table 4) were performed using Type 343. Furthermore, the MIX number and charge/discharge energy are used to examine the advantage of the recommended grid size in terms of calculation accuracy and time.

Table 3
Recommended grid size for different height.

Height from PTES bottom (m)	Grid size (m)
13–16	0.04
9–13	0.06
0–9	0.1

Table 4
Grid size distributions.

Total nodes number	Node size distribution
400	0.04 m from bottom to top
226	0.04 m from 13 m to 16 m; 0.06 m from 9 m to 13 m; 0.1 m from 0 m to 9 m;
160	0.1 m from bottom to top
20	PTES is divided into 20 equal volumes

4.2.1. MIX number

The MIX number was calculated according to Eq. (14) and (15) [55].

$$\mathrm{MIX} = \frac{M_E^{stratified} - M_E^{exp}}{M_E^{stratified} - M_E^{fully-mixed}} \tag{14}$$

$$M_E^{exp} = \sum_{i=1}^{n} z_i \bullet \left(\rho_i \bullet V_i \bullet c_p \bullet T_i\right) \tag{15}$$

where $M_E^{stratified}$ represents the energy momentum for perfectly stratified conditions and $M_E^{fully-mixed}$ represents the energy momentum for thoroughly mixed conditions. M_E^{exp} is calculated based on actual temperature distribution inside PTES. For calculating the MIX, the moment of energy must be calculated for each of the nodes in the PTES [53]. Therefore MIX number can indirectly reflect the PTES temperature calculation accuracy.

Fig. 13 exhibits the development of the MIX number of the Dronninglund PTES from 2015 to 2017. As depicted in this Figure, the MIX number using 20 nodes over three years deviates significantly in March and from June to August. With decreasing the node size to 0.1 m (i.e.,

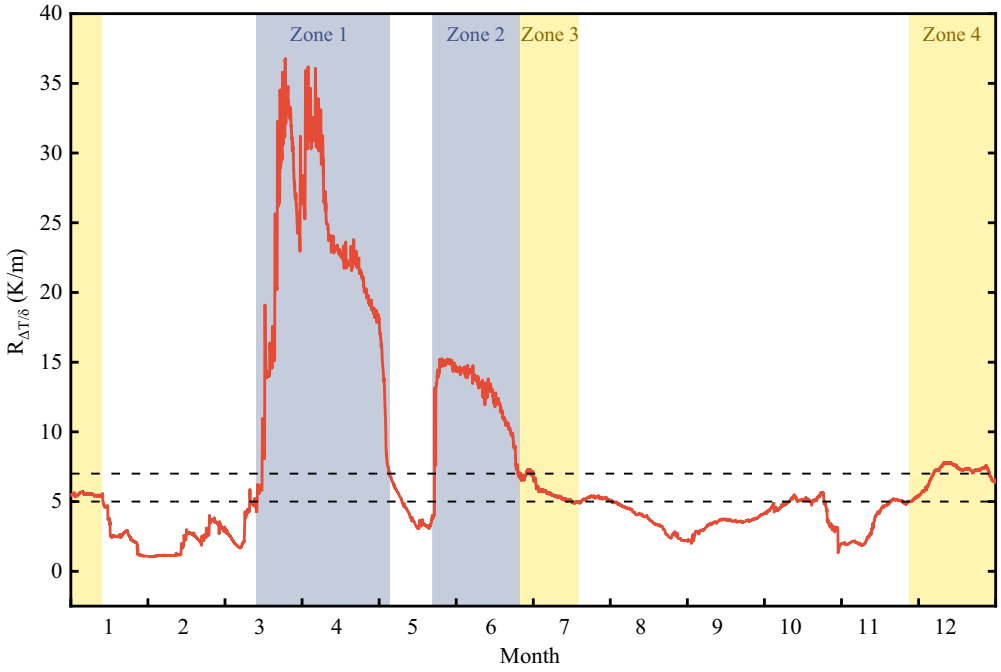

Fig. 12. Annual variation of $R_{\Delta T/\delta}$.

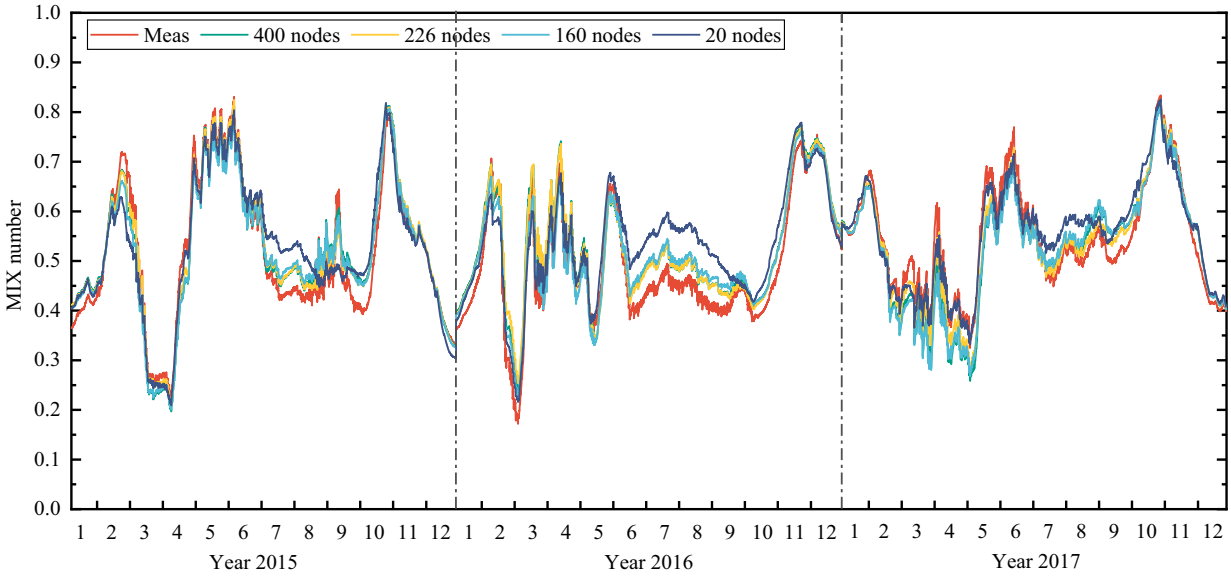

Fig. 13. Development of calculated and measured MIX number 2015–2017.

160 nodes in total), the difference in MIX number between the measurement and the calculation is getting smaller. According to the recommended node sizes, further reducing the node size for positions above 9 m inside the PTES (i.e., 226 nodes in total), an improvement of the MIX number of 0.01 can still be observed. However, reducing the node size to 0.04 m (i.e., 400 nodes in total) seems to have the same calculation accuracy as the recommended node sizes.

Reducing the grid size can improve the calculation accuracy for two reasons. One of the reasons is that as the grid size decreases, temperature distribution can be captured at large $R_{\Delta T/\delta}$, allowing accurate heat transfer calculation between adjacent nodes. Another reason is related to how Type 343 calculates the temperature of the inlet node. As shown in Eq. (14), the temperature of the node at the inlet in a time step depends on the inlet mass flow rate and the mass content of the node. A false numerical diffusion will be introduced in the calculation, and the magnitude of the false diffusion decreases with a decrease in grid size (layer volume). When charging with a significant mass flow rate of higher temperature from June to August, the false numerical diffusion overestimates the mixing effect with a large grid size (20 nodes), resulting in an overestimated MIX number. A decrease in the grid size will significantly improve prediction accuracy for the MIX number.

$$T_{n,i+1} = m_{inlet}T_{inlet}/m_n + \left((m_n - m_{inlet})^{*}T_{n,i}\right)/m_n \tag{14}$$

Table 5 shows the model accuracy assessed by RMSD of the MIX number and the calculation time used for the one-year simulation. This highlights that reduction of RMSD is significant using the recommended grid size distribution (i.e., 226 nodes in total), and it can reach 43 %, 37 %, and 11 % for 2015, 2016, and 2017 respectively. Moreover, refinement of grid size with the same size along the PTES height does not necessarily lead to desired results, increasing computation time.

Table 5
Model accuracy and calculation time under different grid size distribution.

Total node number	RMSD (2015)	RMSD (2016)	RMSD (2017)	Calculation time/ per year
400	0.0339	0.0381	0.0475	68 min
226	0.0288	0.0395	0.0326	26 min
160	0.0369	0.0366	0.0510	14 min
20	0.0505	0.0631	0.0368	3.5 min

4.2.2. Charge/discharge energy

When planning a solar district heating system with PTES, energy flow is another critical factor influencing the selection of auxiliary energy units [13]. Fig. 14 shows the monthly charge/discharge energy with different node numbers compared to the measurement. Therein, the positive values present the charge energy, whereas the negative values present the discharge energy. Note that the relative deviation ratio for charge and discharge energy compared to measurement follows Eq. (16) and (17).

$$\vartheta_{ch} = \left(E_{ch,meas} - E_{ch,calc}\right)/E_{ch,meas} \tag{16}$$

$$\vartheta_{disch} = \left(E_{disch,meas} - E_{disch,calc}\right)/E_{disch,meas} \tag{17}$$

As depicted in Fig. 14, the maximum relative deviation ratio of monthly charged/discharged energy in these three years can be reduced to less than 5 % by increasing the node number. Remarkably, node number 226 also outperforms node numbers 160 and 400 in monthly energy flow, as it is discovered that in some months. For example, in February and December 2016, as well as March and November 2017, the calculation deviations of node numbers 160 and 400 are higher than that of node number 226.

Overall, the recommended grid size has significantly improved the calculation accuracy of TRNSYS Type 343 in terms of PTES temperature distribution and energy quantities, proving the reliability of the proposed grid size selection based on $R_{\Delta T/\delta}$. However, there is still a small difference between the measurement and the improved model, which can be further reduced by considering the inlet mixing effect.

5. Conclusion

This study developed a full-scale 3D CFD model of PTES including water and soil regions. The proposed CFD model was calibrated using measurements of the Dronninglund PTES. The CFD model was used to determine the optimal grid size for the 1D PTES model. The influence of grid size on the prediction accuracy of the 1D PTES model was examined. The major conclusions are summarized as follows:

1) The difference between the measured and the calculated temperatures for the soil and water region is less than 2 K and 1 K, respectively. In addition, the energy flow is in good agreement with the measurements, with a maximum temperature difference of 3 K and a maximum mass flow rate difference of 10 kg/m^3 between

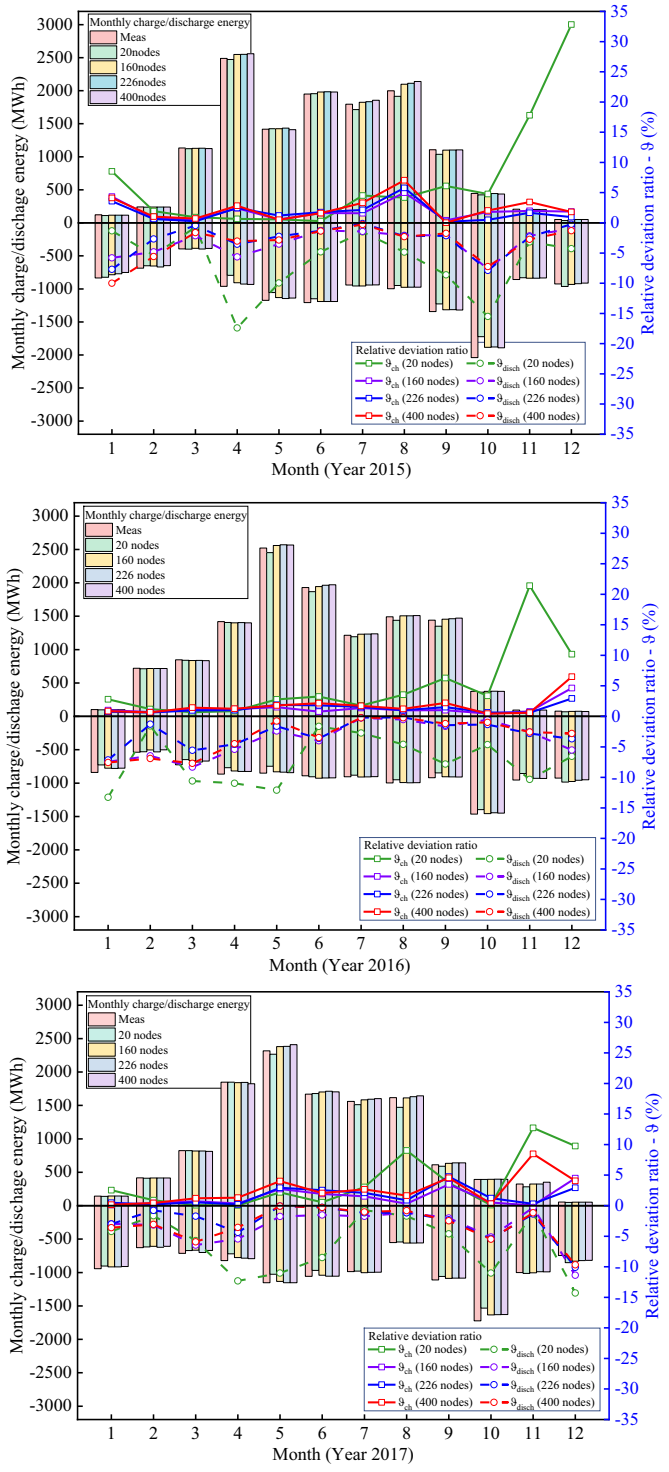

Fig. 14. Monthly charge/discharge energy under different node sizes compared with measurement.

measurements and CFD calculation. Therefore, the accuracy of the 3D model is considered acceptable.

2) Grid size in the horizontal directions has a negligible effect on temperature distribution prediction, but the vertical grid size has a considerable impact. For cases with significant temperature differences within a thinner thermocline thickness, the reduction in RMSD can reach 50 % by reducing the grid size. The temperature gradient of the thermocline $R_{\Delta T/\delta}$ is proposed as a criterion to guide the grid size selection for 1D multi-node models.

3) An optimal grid size distribution was determined by analyzing the dynamic variation characteristics of the thermocline throughout the year. A three-year simulation was performed on a multi-node model TRNSYS Type 343 to verify the reliability of choosing the appropriate grid size distribution using $R_{\Delta T/\delta}$. The calculation accuracy using the appropriate grid size distribution is superior to other grid size distributions in both temperature distribution and energy flow. The RMSD reduction in MIX numbers in 2015, 2016, and 2017 can reach 43 %, 37 %, and 11 %, respectively. Moreover, the monthly charge/discharge energy deviation ratio can be reduced to less than 5 %.

Further, two aspects are proposed for future work:

i) Aside from the influence of grid size analyzed above, the mixing effect around the diffusers caused by inlet jet flow should also be investigated.

ii) Despite the model's ability to predict soil temperature, the influence of groundwater on the heat loss of the PTES remains unknown. The CFD model could be used to develop a simplified 1D PTES model considering the influence of groundwater.

CRediT authorship contribution statement

Yutong Xiang: Research, Writing.
Meng Gao: Reviewing.
Simon Furbo: Supervision, reviewing.
Dengjia Wang: Reviewing.
Zhiyong Tian: Reviewing.
Jianhua Fan: Fund raising, idea formulation, editing.

Declaration of competing interest

None.

Data availability

Data will be made available on request.

Acknowledgments

The work is partly funded by the National Key R&D Program of China (No. 2021YFE0113500), the Danish Energy Agency EUDP project for participation of the IEA ECES Annex 39: "Large Thermal Energy Storages for District Heating" (no. 64020-2036) and the Chinese Scholarship Council (CSC) (No. 201909110075). Without their support, the research would not be possible.

References

[1] IRENA, Innovation outlook: thermal energy storage, International Renewable Energy Agency, Abu Dhabi, 2020. https://www.irena.org/-/media/Files/IRENA/Agency/Publication/2020/Nov/IRENA_Innovation_Outlook_TES_2020.pdf.
[2] V. Lottner, M.E. Schulz, E. Hahne, Solar-assisted district heating plants: status of the german programme Solarthermie-2000, Sol. Energy 69 (2000) 449–459, https://doi.org/10.1016/S0038-092X(00)00125-0.
[3] P.A. Sørensen, Best practice for implementation and operation of large scale borehole and pit heat thermal storages, Planenergi (2019) 1–22.
[4] T. Schmidt, T. Pauschinger, P.A. Sørensen, A. Snijders, R. Djebbar, R. Boulter, et al., Design aspects for large-scale pit and aquifer thermal energy storage for district heating and cooling, Energy Procedia 149 (2018) 585–594, https://doi.org/10.1016/j.egypro.2018.08.223.
[5] D. Mangold, Seasonal storage - a German success story, Sun & Wind Energy 1 (2007) 48–58.
[6] A. Dahash, F. Ochs, G. Giuliani, A. Tosatto, Understanding the interaction between groundwater and large-scale underground hot-water tanks and pits, Sustain. Cities Soc. 71 (2021), 102928, https://doi.org/10.1016/j.scs.2021.102928.
[7] J.A. Duffie, W.A. Beckman, J. McGowan, Solar Engineering of Thermal Processes vol. 53, American Journal of Physics, 1985.

[8] A.V. Novo, J.R. Bayon, D. Castro-Fresno, J. Rodriguez-Hernandez, Review of seasonal heat storage in large basins: water tanks and gravel-water pits, Appl. Energy 87 (2010) 390–397, https://doi.org/10.1016/j.apenergy.2009.06.033.

[9] M. Mahmoud, M. Ramadan, S. Naher, K. Pullen, A. Baroutaji, A.G. Olabi, Recent advances in district energy systems: a review, Therm. Sci. Eng. Prog. 20 (2020), 100678, https://doi.org/10.1016/j.tsep.2020.100678.

[10] T. Yang, W. Liu, G.J. Kramer, Q. Sun, Seasonal thermal energy storage: a techno-economic literature review, Renew. Sustain. Energy Rev. 139 (2021), 110732, https://doi.org/10.1016/j.rser.2021.110732.

[11] Y. Xiang, Z. Xie, S. Furbo, D. Wang, M. Gao, J. Fan, A comprehensive review on pit thermal energy storage: technical elements, numerical approaches and recent applications, J. Energy Storage (2022). Submitted for publication.

[12] A. Dahash, F. Ochs, M.B. Janetti, W. Streicher, Advances in seasonal thermal energy storage for solar district heating applications: a critical review on large-scale hot-water tank and pit thermal energy storage systems, Appl. Energy 239 (2019) 296–315, https://doi.org/10.1016/j.apenergy.2019.01.189.

[13] A. Dahash, F. Ochs, A. Tosatto, W. Streicher, Toward efficient numerical modeling and analysis of large-scale thermal energy storage for renewable district heating, Appl. Energy 279 (2020), 115840, https://doi.org/10.1016/j.apenergy.2020.115840.

[14] A. Dahash, M.B. Janetti, F. Ochs, Detailed axial symmetrical model of large-scale underground thermal energy storage, in: Proceedings of COMSOL 2018 Conference, Lausanne, 2018.

[15] A. Dahash, M.B. Janetti, F. Ochs, Detailed 3-D mdels of a large-scale underground thermal energy storage with consideration of groundwater conditions, in: International Sustainable Energy Conference, Graz, 2018, pp. 597–604.

[16] A. Dahash, M.B. Janetti, F. Ochs, Numerical analysis and evaluation of large-scale hot water tanks and pits in district heating systems, in: 16th IBPSA International Conference and Exhibition, 2019, pp. 1692–1699.

[17] S. Raab, D. Mangold, H. Müller-Steinhagen, Validation of a computer model for solar assisted district heating systems with seasonal hot water heat store, Sol. Energy 79 (2005) 531–543, https://doi.org/10.1016/j.solener.2004.10.014.

[18] G. Gauthier, Benchmarking, and improving models of subsurface heat storage dynamics. Comparison of Danish PTES and BTES installation measurements with their corresponding TRNSYS models, in: vol. 47, GEOTHERMICA-ERA NET Cofund Geothermal, 2020.

[19] X. Pan, Y. Xiang, M. Gao, J. Fan, S. Furbo, et al., Long-term thermal performance analysis of a large-scale water pit thermal energy storage, J. Energy Storage 52 (2022), 105001, https://doi.org/10.1016/j.est.2022.105001.

[20] Z. Xie, Y. Xiang, D. Wang, O. Kusyy, W. Kong, S. Furbo, et al., Numerical investigations of long-term thermal performance of a large water pit heat storage, Sol. Energy 224 (2021) 808–822, https://doi.org/10.1016/j.solener.2021.06.027.

[21] Y. Bai, M. Yang, J. Fan, X. Li, L. Chen, G. Yuan, et al., Influence of geometry on the thermal performance of water pit seasonal heat storages for solar district heating, Build. Simul. 14 (2020) 579–599, https://doi.org/10.1007/s12273-020-0671-9.

[22] Y. Bai, Z. Wang, J. Fan, M. Yang, X. Li, L. Chen, et al., Numerical and experimental study of an underground water pit for seasonal heat storage, Renew. Energy 150 (2020) 487–508, https://doi.org/10.1016/j.renene.2019.12.080.

[23] J. Fan, J. Huang, O.L. Andersen, S. Furbo, Thermal performance analysis of a solar heating plant, in: Solar World Congress 2017, Abu Dhabi, United Arab Emirates, 2017, pp. 291–300.

[24] K.M. Powell, T.F. Edgar, An adaptive-grid model for dynamic simulation of thermocline thermal energy storage systems, Energy Convers. Manag. 76 (2013) 865–873, https://doi.org/10.1016/j.enconman.2013.08.043.

[25] L. Mazzarella, Multi-flow stratified thermal storage model with full-mixed layers PdM-XST, Department of Mathematical Physics University of Lund, 1992. https://www.trnsys.de/static/d747464ad7627a47af6610ab89da64e9/Type_342_en.pdf.

[26] C. Unrau, Numerical investigation of one-dimensional storage tank models and the development of analytical modelling techniques, McMaster University, Canada, 2017.

[27] S.A. Klein, W.A. Bechman, J.W. Mitchell, et al., TRNSYS 17 a transient system simulation program volume 4 mathematical reference, Solar Energy Laboratory, University of Wisconsin-Madison, U.S.A, 2009. http://web.mit.edu/parmstr/Public/TRNSYS/04-MathematicalReference.pdf.

[28] PlanEnergi, Sunstore 3. Fase 1: Projektering og udbud, 2011. https://energiforskning.dk/sites/energiforskning.dk/files/slutrapporter/slutrapport_incl._bilag_1_12042011_1824.pdf.

[29] A.J. Kallesøe, T. Vangkilde-Pedersen, et al., Underground thermal energy storage (UTES)-state-of-the-art, example cases and lessons learned, in: HEATSTORE project report, GEOTHERA NET Cofund Geothermal, 2019, 130 pp + appendices.

[30] M.V. Jensen, PlanEnergi, Task 45 large systems seasonal pit heat storages - guidelines for materials & construction, Solar Heating & Cooling Programme International Energy Agency, 2014. http://task45.iea-shc.org/data/sites/1/publications/IEA-SHC%20T45.B.3.2%20TECH%20Seasonal%20storages%20-%20Water%20Pit%20Guidelines.pdf.

[31] NIRAS, Rørindføring alternativ 2. Sunstore 3 Dronninglund Fjernvarme, in: CAD File, 2010.

[32] AEA, Dampvarmelager snit, in: Dronninglund Fjernvarme. Projekt 13005. CAD File, Averhoff Energi Anlæg A/S, 2013.

[33] M.V. Jensen, J.D. Andersen, Dronninglund. Lunderbjerg damvarmelager måling af grundvandstemperatur, in: Geo projekt nr.37304, GEO, Denmark, 2015.

[34] ANSYS, Fluent theory guide, ANSYS, Inc, U.S.A., 2019.

[35] J.D. Chung, S.H. Cho, C.S. Tae, H. Yoo, The effect of diffuser configuration on thermal stratification in a rectangular storage tank, Renew. Energy 33 (2008) 2236–2245, https://doi.org/10.1016/j.renene.2007.12.013.

[36] R. Blevins, Applied fluid dynamic handbook, Krieger Pub Co, 1984.

[37] Y. Deng, D. Sun, M. Niu, B. Yu, R. Bian, Performance assessment of a novel diffuser for stratified thermal energy storage tanks - the nonequal-diameter radial diffuser, J. Energy Storage 35 (2021), 102276, https://doi.org/10.1016/j.est.2021.102276.

[38] G.H. Keulegan, Interfacial instability and mixing in stratified flows, J. Res. Natl. Bur. Stand. (U.S.) 43 (1949) 487–500, https://doi.org/10.6028/jres.043.041.

[39] L. Cai, W.E. Stewart Jr., C.W. Sohn, Turbulent buoyant flows into a two dimensional storage tank, Int. J. Heat Mass Transfer 36 (1993) 4247–4256, https://doi.org/10.1016/0017-9310(93)90087-M.

[40] J. Song, W.P. Bahnfleth, J.M. Cimbala, Parametric study of single-pipe diffusers in stratified chilled water storage tanks (RP-1185), in: HVAC and R Research 10, 2004, pp. 345–365, https://doi.org/10.1080/10789669.2004.10391108.

[41] R. Manimaran, Performance assessment of solar PV and thermal-driven humidification dehumidification systems: a CFD modelling approach, Energy Convers. Manag. 245 (2021), 114574, https://doi.org/10.1016/j.enconman.2021.114574.

[42] J. Fan, J. Huang, A. Chatzidiakos, S. Furbo, Experimental and theoretic investigations of thermal behavior of a seasonal water pit heat storage, in: Solar World Congress 2017, Abu Dhabi, United Arab Emirates, 2017, pp. 714–725.

[43] A. Chatzidiakos, CFD calculations for solar water pond heat storages, Technical University of Denmark, Denmark, 2016.

[44] I.N. Hamdhan, B.G. Clarke, Determination of thermal conductivity of coarse and fine sand soils, Proceedings World Geothermal Congress 2010. Baili, Indonesia (2010), https://doi.org/10.1137/120866701.

[45] M.A. Pagola, R.L. Jensen, S. Madsen, S.E. Poulsen, Measurement of thermal properties of soil and concrete samples, in: DCE Technical Reports No.235, Aalborg University. Department of Civil Engineering, Denmark, 2017.

[46] A. Łukawska, G. Ryżyński, M. Żeruń, Serial laboratory effective thermal conductivity measurements of cohesive and non cohesive soils for the purpose of shallow geothermal potential mapping and databases - methodology and testing procedure recommendations, Energies 13 (2020), 914.

[47] NMC, Nomalen 28N, NMC Termonova Oy, 2015. https://dms.etra.fi:9900/72192/conversions/original?version=0.

[48] K.A. Thakare, H.G. Vishwakarma, A.G. Bhave, Experimental investigation of possible use of HDPE as thermal storage material in thermal storage type solar cookers, Int. J. Eng. Res. Technol. 04 (2015) 92–99, https://doi.org/10.15623/ijret.2015.0412019.

[49] SOLMAX, Produktinformation hypernet, SOLMAX GEOSYNTHETICS GMBH, http://downloads.solmaxgeosynthetics.com/SOLMAX%20HyperNet.pdf.

[50] J. Dannemand Andersen, L. Bødker, M.V. Jensen, Large thermal energy storage at Marstal district heating, in: vol. 4, 18th International Conference on Soil Mechanics and Geotechnical Engineering, Paris, 2013, pp. 3351–3354.

[51] F. Ochs, W. Heidemann, H. Müller-Steinhagen, Effective thermal conductivity of moistened insulation materials as a function of temperature, Int. J. Heat Mass Transfer 51 (2008) 539–552, https://doi.org/10.1016/j.ijheatmasstransfer.2007.05.005.

[52] C. Winterscheid, Dronninglund district heating monitaring data evaluation for the years 2015-2017, Steinbeis Research Institute for Solar and Sustainable Thermal Energy Systems, 2017.

[53] I. Sifnaios, A.R. Jensen, S. Furbo, J. Fan, Performance comparison of two water pit thermal energy storage systems using energy, exergy, and stratification indicators, J. Energy Storage 52 (2022) 104947, https://doi.org/10.1016/j.est.2022.104947.

[54] C. Xu, M. Liu, S. Jiao, H. Tang, J. Yan, Experimental study and analytical modeling on the thermocline hot water storage tank with radial plate-type diffuser, Int. J. Heat Mass Transfer 186 (2022), 122478, https://doi.org/10.1016/j.ijheatmasstransfer.2021.122478.

[55] M.Y. Haller, C.A. Cruickshank, W. Streicher, S.J. Harrison, E. Andersen, S. Furbo, Methods to determine stratification efficiency of thermal energy storage processes - review and theoretical comparison, Sol. Energy 83 (2009) 1847–1860, https://doi.org/10.1016/j.solener.2009.06.019.